Journal of Materials Chemistry A

ROYAL SOCIETY OF CHEMISTRY

PAPER

Published on 28 July 2026

Cite this: DOI: 10.1039/d6ta04062d

Single-atom Fe–N_x–C electrocatalysts for efficient nitrate reduction reaction

Simone Lombardi,[a] Lucia Codega,[a] Mohsin Muhyuddin,[a] Nicola Lisi,[b] Valerio Ficca,[b] Alessandro Lavacchi,[c] Enrico Berretti,[c] Matteo Spotti,[a] Giovanni Di Liberto,[a] Francesco Paparoni,[d] Javid Rezvani,[e] Rosanna Viscardi *[b] and Carlo Santoro *[a]

Iron–nitrogen–carbons (Fe–N_x–Cs) emerged as highly efficient single-atom electrocatalysts (ECs) for the nitrate reduction reaction (NO_3RR), yet the structural evolution of their active sites during pyrolysis remains a critical area of investigation. In this work, we systematically investigate the thermal stability and transformation of Fe–N_x active sites derived from iron(II)-phthalocyanine (FePc) supported over conductive carbon black (Ketjen Black ec-600JD) during pyrolysis from room temperature (RT) to 600 °C. The primary objective is to evaluate how the pyrolysis temperature, from RT to 600 °C in N_2/H_2 atmosphere, dictates the evolution of these sites and correlates with the electrochemical performance toward NO_3RR in neutral pH electrolytes. Utilizing a combination of advanced spectroscopic and microscopic techniques (XAS, XPS, BF-STEM, XRD and Raman), we tracked the transition of iron species from molecular precursors to integrated active phases. While BF-STEM and XAS detect the formation of sub-nanometric clusters and metallic nanoparticles at 500–600 °C, the faradaic efficiency (FE) for ammonia remains consistently above 75% at −0.8 V *vs.* RHE. However, the best electrocatalytic activity was observed for the EC pyrolyzed at 300 °C. Principal Component Analysis (PCA) and quantum chemical simulations were used to unravel the complex correlations between the structural evolution of the iron sites and the electrochemical performance. The results identify the Fe–N_3 configuration as the primary active site responsible for maintaining a high FE for NH_4^+ at high overpotentials, successfully outcompeting the concurrent hydrogen evolution reaction (HER). This study provides fundamental insights into the structure–activity relationships of single-atom Fe–N_x–C ECs derived from FePc for the NO_3RR.

Received 13th May 2026
Accepted 28th July 2026

DOI: 10.1039/d6ta04062d

rsc.li/materials-a

1. Introduction

Ammonia (NH_3) has a global production exceeding 176 million metric tonnes[1] and it stands as the world's second most produced chemical. While approximately 80% of NH_3 serves as a precursor for fertilizer,[2] specifically urea (CH_4N_2O), being the most used nitrogen-based fertilizer worldwide,[3] ammonia remains essential for various industries, including plastics, pharmaceuticals, refrigeration, and explosives.[4] However, the conventional Haber–Bosch process, responsible for over 96% of global production, is a major energy consumer and accounts for approximately 1.2% of anthropogenic carbon dioxide (CO_2) emissions.[5] The electrochemical nitrogen reduction reaction (NRR) has emerged as a promising sustainable alternative.[6] However, its development is hindered by the high dissociation energy of the N≡N bond (941 kJ mol^{-1}) and the poor mass transport of N_2 due to its limited solubility in aqueous electrolytes (0.71 mmol L^{-1}).[7]

In contrast, the nitrate anion (NO_3^-) has been recognized as a more attractive N-source thanks to the lower dissociation energy of N=O (204 kJ mol^{-1}) and higher solubility (10.4 mol L^{-1}) in water.[8] NO_3^- sources primarily originate from industrial and agricultural wastewater, with concentrations reaching up to 2 M (124 g L^{-1}).[9] Therefore, the fundamental motivation for the electrochemical nitrate reduction reaction (NO_3RR) to utilize NO_3^- derived from wastewater while simultaneously synthesizing NH_3 sustainably. In principle, if this process is powered by renewable energy, it can potentially become a sustainable and low-carbon process.

The electrochemical conversion of NO_3^- to NH_3 involves an eight-electron transfer mechanism, multiple reaction intermediates and by-products such as N oxides, N_2 and NO_2^-.[10] Furthermore, NO_3RR is generally conducted at a potential

[a]Department of Materials Science, University of Milano-Bicocca, U5, Via Roberto Cozzi 55, 20125, Milano, Italy. E-mail: carlo.santoro@unimib.it

[b]Casaccia Research Center, ENEA, Department of Energy Technologies and Renewable Sources, Via Anguillarese 301, 00123, Santa Maria di Galeria, Rome, Italy. E-mail: rosanna.viscardi@enea.it

[c]Istituto di Chimica Dei Composti OrganoMetallici (ICCOM), Consiglio Nazionale Delle Ricerche (CNR), Via Madonna Del Piano 10, 50019, Sesto Fiorentino, Firenze, Italy

[d]Synchrotron SOLEIL, L'Orme des Merisiers, 91190 Saint-Aubin, France

[e]Physics Division, School of Science and Technology, University of Camerino, Via Madonna Delle Carceri 9, 62032 Camerino, MC, Italy

overlapping with the competitive hydrogen evolution reaction (HER), reducing the faradaic efficiency (FE) of ammonia production.

Consequently, developing efficient platinum group metal-free (PGM-free) materials is crucial for improving both the activity and selectivity towards the desired product. Current research prioritizes ECs with minimized metal content to ensure industrial scalability and environmental safety.[11]

In this context, carbon-based materials with atomically dispersed transition metals (TMs) of the type TM–N_x–C, maximize metal utilization efficiency while providing high electrocatalytic activity and selectivity through fully exposed active sites.[12,13] Originally pioneered for the oxygen reduction reaction (ORR),[14,15] these materials were subsequently adapted for the carbon dioxide reduction (CO_2RR),[16,17] and have recently gained attention for the NO_3RR[18]

While boron, fluorine, and phosphorus have also been explored as potential candidates, nitrogen is the preferred heteroatom due to its high electrical conductivity[19] and an electronegativity/atomic size comparable to carbon, which facilitates the formation of stable configurations within the carbon lattice.[20]

These nitrogen configurations are typically categorized into pyridinic-N, pyrrolic-N, graphitic-N, and pyridinic-N-oxide. While pyridinic and pyrrolic N-moieties are typically involved in coordinating the metal center, the graphitic nitrogen distributed within the carbon lattice acts as a promoter for NO_3^- adsorption by inducing an asymmetric charge distribution on the carbon scaffold.[21]

In a systematic screening of 14 different M–N_x–C electrocatalysts (ECs) across the 3d, 4d, 5d, and f-block elements, Murphy *et al.*[18] identified Fe–N_x–C as one of the most promising candidates for the NO_3RR.

Beyond its superior intrinsic activity, iron is earth-abundant, low-cost, and environmentally benign.[22] Wu *et al.*[9] reported the first case of NO_3RR using Fe–N_x–C, achieving a yield rate of 20 mg h^{-1} $mg_{cat}{}^{-1}$ and a FE of approximately 75%. Subsequently, other strategies emerged: single-atom Fe sites embedded in g-C_3N_4 achieved a FE of 77.3% even at low NO_3^- concentration (50 ppm),[23] while Li *et al.*[24] demonstrated a polymer-hydrogel strategy to produce N-coordinated Fe sites that reached a maximum NH_3 yield rate of 2.75 mg_{NH_3} h^{-1} cm^{-2} with nearly 100% FE.

Fe–N_x–C ECs are widely studied for ORR to substitute platinum-based ECs, and these ECs are quite active, especially in alkaline electrolytes.[25] There are different ways of synthesizing single-atom Fe–N_x–C ECs as reported in a recent review.[26] The first one is based on mixing nitrogen-rich organic precursor with iron salt, pyrolyzing them at controlled temperature and atmosphere and then doing an acid washing to remove the metallic nanoparticles.[27–30] Eventually, hard [31–34] or soft [35–37] templating is used for creating a hierarchically carbon structure that supports the Fe–N_x–C active sites. This method uses a thermal treatment that takes place in a controlled atmosphere without any involvement of oxygen, which is considered the only reliable methodology to induce favorable and robust active sites in Fe–N_x–C with atomic-level homogeneity.[38] The second method is based on the fabrication of covalent organic frameworks (COFs) that are built and then subjected to pyrolysis to enhance the electrical conductivity of the support while leaving the active sites of the type Fe–N_x–C on the surface.[39–41] The third method relies on the fabrication of metal organic frameworks (MOFs) that are constituted by metallic nodes coordinated with metallic ligands.[42] Also in this case, the pyrolytic process converts the organics into conductive carbon, leaving the metal atomically dispersed in the desired form.[43] The fourth method relies on the usage of molecular ECs and particularly metal-containing azamacrocycles (Fe–N_x–C) such as phthalocyanine, porphyrins, *etc.* that are mixed with conductive carbon matrices and then subjected to pyrolysis to integrate them to the conductive substrate.[44–47]

In this work, we systematically investigated the structural transformation of Fe–N_x–C EC derived from the heat treatment of iron(II)-phthalocyanine (FePc) supported on conductive carbon black. The heat treatment occurred across various controlled temperatures ranging from RT to 600 °C, with a 100 °C step, in a slightly reducing atmosphere of N_2/H_2.

Advanced spectroscopic and microscopic techniques such as X-ray absorption spectroscopy (XAS), X-ray photoelectron spectroscopy (XPS), scanning transmission electron microscopy (STEM), X-ray diffraction (XRD) and Raman spectroscopy were used to characterize the evolution of active site structure, including surface chemistry and morphology of the synthesized ECs. The progression of the iron species from their molecular origin to the formation of nanoparticles was evaluated across the range of pyrolysis temperature. The structure–property relationship throughout the pyrolysis process was elucidated and supported by computational work (density functional theory, DFT), identifying the critical temperature thresholds that maximize NO_3RR activity.

2. Experimental

2.1. Synthesis

The different ECs were prepared by blending of 20 wt% FePc with 80 wt% of commercial carbon black (Ketjenblack EC-600JD, KJB) using high-energy ball milling for 1 h at a rotation speed of 400 rpm. The resulting homogeneous mixture, which was labeled as RT (room temperature), was then poured into a cleaned alumina boat and transferred to a quartz tube with an atmosphere-controlled flange system, integrated into a horizontal tube furnace.

Before initiating pyrolysis, the quartz tube underwent a gas purge with N_2/H_2 gas (95 vol% nitrogen balanced with 5 vol% hydrogen) for at least 30 min to eliminate air from the system. Subsequently, the samples underwent pyrolysis at specified temperatures (100, 200, 300, 400, 500 and 600 °C) for 1 h, with heating and cooling ramp rates maintained at 600 °C h^{-1}.

The samples obtained were named according to their pyrolysis temperatures using the format "Fe_temperature". For example, the sample with a pyrolysis temperature of 600 °C was labelled "Fe_600". The sample not pyrolyzed was labelled as Fe_RT.

2.2. Characterizations

XRD analysis was carried out using a Rigaku Miniflex 600 diffractometer equipped with a copper anode (operated at 40 kV and 15 mA). Diffraction patterns were collected within the 2θ range of 10° to 80°, employing a scan step of 0.01° and a scanning speed of 5.0° per minute. Phase identification was conducted by matching the experimental patterns with standard reference data from the ICDD database, using the PDXL-2 software suite. The carbon structures were studied through micro-Raman (Jasco Ventuno System) spectroscopy installed with a He–Ne laser ($\lambda = 632.8$ nm). The system was working at 6 kW cm^{-2} power density while the signals were recorded with a Peltier-cooled charge-coupled device camera (kept at −50 °C). Before collecting the main Raman spectra on the Fe–N_x–C, calibration was carried out on a standard silicon single crystal, demonstrating a characteristic peak at 520.65 cm^{-1}. Scanning transmission electron microscopy (STEM) and energy-dispersive X-ray spectroscopy (EDX) analyses were carried out using a Thermo Fisher Talos F200X G2 microscope operating at an accelerating voltage of 200 kV. The EDX maps were taken with a Super X spectrometer equipped with four 30 mm^2 silicon drift detectors with a collection angle of 0.7 srad. Data processing and arrangement have been performed with the Thermofisher proprietary software VELOX.

Samples consisting of pellets of pure powders were probed using XAS at the SAMBA beamline, collecting Fe K-edge spectra in transmission mode. Spectra were normalized to the incident photon flux and calibrated in energy using a metallic Fe reference, fixing the first inflection point to 7112 eV. Data normalization and linear combination fitting were carried out using the software Fastosh.[48] Pre-edge peak was analyzed using LARCH, following a similar methodology discussed elsewhere,[49] using a linear + Lorenzian background function and deconvoluting the peak with Pseudo-Voigt functions: Fe^{2+}–N_x (7113.2 eV), Fe^{3+}–N_x (7114.4 eV) and 7118 eV for Fe–N_4 in tetragonal (D_{4h}) geometry, as indicated by Choi *et al.*[50]

Finally, XPS analysis was executed in Ultra High Vacuum (UHV, $<10^{-10}$ mBar) using an Escalab Qxi (Thermofisher) system equipped with monochromatic Al K_α (1486.6 eV) X-ray source and flood gun for standard charge neutralization. The samples were placed over a stainless steel sample holder to acquire the full survey and 4 different core levels, namely C 1s, O 1s, N 1s, and Fe 2p. The pass energy was set to 20 eV for C 1s, O 1s and N 1s, and to 30 eV for Fe 2p. The fittings were performed using Kalibri KolXPD software constraining the fits over the reference sample. The multiplet splitting of the Fe 2p core level has been accounted using broader peaks and reconducting the deconvolution to two main contributions with related satellites.

2.3. Preparation of the working electrode

The EC ink was prepared by dispersing 5 mg of EC powder in a solution containing 670 μL of isopropanol (IPA), 300 μL of Milli-Q water, and 30 μL of a 5 wt% Nafion solution. The suspension was sonicated in an ultrasonic bath for 15 minutes, followed by probe sonication for 1 hour using a pulsed mode (5 s on/5 s off) at 30% amplitude. For linear sweep voltammetry (LSV) measurements, 19.6 μL of the EC ink was drop-cast onto a glassy carbon disk of a rotating disk electrode (RDE) having a geometric area of 0.1962 cm^2), resulting in an EC loading of 0.5 mg cm^{-2}. For chronoamperometry (CA) experiments, a TGP-H-60 carbon paper (thickness: 0.20 ± 0.05 mm) was used as received, without any pre-treatment. A volume of 100 μL of EC ink was drop-cast on the carbon paper with a 1 cm^2 geometric working area for an EC loading of 0.5 mg cm^{-2}.

2.4. Linear sweep voltammetry

To evaluate both the HER and NO_3RR activity, LSVs were performed. All measurements were carried out using a Biologic potentiostat in a single-compartment electrochemical cell equipped with an RDE rotator. A RDE was employed as the working electrode, with a graphite rod as the counter electrode and a reversible hydrogen electrode (RHE) as the reference. HER activity was measured in a 0.1 M phosphate buffer solution (PBS) composed of 0.074 M KH_2PO_4 and 0.026 M K_2HPO_4. For NO_3RR measurement, the electrolyte consisted of 0.1 M PBS with an additional 0.16 M NO_3^- (KNO_3). The pH of the electrolyte was set to 6.3.

Before the electrochemical measurements, Ar gas was purged into the cell for 30 min at 80 sccm and maintained at 20 sccm during the tests. Prior to LSV, cyclic voltammetry (CV) was performed in the potential range from 0 V to −1 V *vs.* RHE, at a scan rate of 50 mV s^{-1} and a rotation speed of 1600 rpm, until stable polarization curves were obtained. Subsequently, LSV was conducted (0 V to −1 V, 20 mV s^{-1}, 1600 rpm). The reported curves represent the average of these three measurements. Note that the applied potentials for all electrochemical tests were *iR* corrected.

2.5. Chronoamperometry

Electrochemical nitrate reduction measurements were carried out in a two-compartment H-type cell, separated by an Aquivion® E87-12 S proton exchange membrane (PEM) used as received without pre-treatment. All measurements were conducted using a Biologic potentiostat. A standard three-electrode system was used with a reversible hydrogen electrode (HydroFlex®) and a graphite rod as the reference and counter electrode, respectively. The electrolyte used for all NO_3RR experiments is a 0.1 M PBS with an additional 0.16 M NO_3^- (KNO_3).

Both the working and counter chambers were filled with 40 mL of electrolyte. The pH of the electrolyte was set to 6.3 to ensure that the produced ammonium (NH_4^+) remains in its protonated form and does not convert to gaseous NH_3, considering the pK_a of NH_4^+ (pK_a: 9.24). This condition allows for accurate quantification of NH_4^+ *via* ion chromatography (IC). Chronoamperometric (CA) tests were performed for 1 hour under constant magnetic stirring (200 rpm), at three different applied potentials: −0.60 V, −0.80 V and −1.0 V *vs.* RHE. Before the electrochemical measurements, Ar gas was purged into the cell for 30 min at 80 sccm and maintained at 20 sccm during the tests.

2.6. Detection and determination of ammonium and nitrite ions

After each electrolysis experiment, aliquots of the catholyte were collected and analyzed for NH_4^+ and NO_2^- concentrations by IC; specifically, for the determination of ammonium, 1 mL of the electrolyte was transferred into a vial and diluted to a final volume of 10 mL (1 : 10 dilution).

For nitrite analysis, 200 μL of electrolyte was diluted to 10 mL (1 : 50 dilution). Chromatographic separation was performed using a Metrohm Eco IC Ion Chromatograph system (Metrohm AG, Herisau, CH), equipped with a conductivity detector, a MSM conductivity suppressor and a Metrohm 863 Compact Autosampler. The IC was equipped with a Metrohm Metrosep A Supp 5 (4 mm × 250 mm) and a Metrosep A Supp 1 Guard/4.6 guard-column for anion separation and with a Metrosep C 6 (4 mm × 250 mm) and a Metrosep C 6 S-guard/4.0 guard-column for cation separation (Metrohm AG, Herisau, CH). For cation analysis, the mobile phase was a 4 mmol L^{-1} HNO_3 + 0.7 mmol L^{-1} oxalic acid aqueous solution, at a flow rate of 0.9 mL min^{-1}, at room temperature (25 °C). For anion analysis, the mobile phase was a 3.2 mmol L^{-1} Na_2CO_3 + 1.0 mmol L^{-1} $NaHCO_3$ aqueous solution, at a flow rate of 0.8 mL min^{-1}, at room temperature (25 °C).

The injection volume was 10 μL. The eluent conductivity background was suppressed by using a Metrohm MSM cation-exchange membrane set in-line after the anionic column (no suppression was used for cation detection). It was regenerated with 100 mmol L^{-1} of sulfuric acid flowing countercurrently at a flow rate of 1.5 mL min^{-1}.

2.7. Calculation of the yield and faradaic efficiency

For the nitrate reduction reaction (NO_3RR), the yield rate of ammonium (NH_4^+) was calculated using eqn (2.1), while the corresponding faradaic efficiency (FE) was determined using eqn (2.2):

$$\text{Yield rate } NH_4^+ = \frac{\text{C } NH_4^+ \times V}{\text{MM } NH_4^+ \times t \times S} \tag{2.1}$$

$$\text{FE } NH_4^+ = \frac{n \times F \times \text{C } NH_4^+ \times V}{\text{MM } NH_4^+ \times Q} \tag{2.2}$$

Similarly, for the partial reduction of nitrate to nitrite (NO_2^-), the yield rate and faradaic efficiency were calculated using eqn (2.3) and (2.4), respectively:

$$\text{Yield rate } NO_2^- = \frac{\text{C } NO_2^- \times V}{\text{MM } NO_2^- \times t \times S} \tag{2.3}$$

$$\text{FE } NO_2^- = \frac{n \times F \times \text{C } NO_2^- \times V}{\text{MM } NO_2^- \times Q} \tag{2.4}$$

where, CNH_4^+ and CNO_2^- are the mass concentrations (mg L^{-1}) of ammonium and nitrite, respectively; V is the volume of the electrolyte in the cathodic compartment; t is the duration of the chronoamperometric experiment (1 h); S is the surface area of the working electrode (1 cm^2); n is the number of electrons transferred, for NO_3^- to NO_2^- is equal to 2, whereas for NO_3^- to NH_4^+ is equal to 8; MM NH_4^+ and MM NO_2^- are the molar masses of ammonium (18.04 g mol^{-1}) and nitrite (46.00 g mol^{-1}), respectively; F is the Faraday's constant (96.485 C mol^{-1}), and Q is the total charge passed during electrolysis, calculated by integrating the current over time during chronoamperometry. Note that all error bars reported in this work represent the standard deviation from triplicate measurements performed using independently prepared electrodes.

2.8. Calculation of the electrochemical surface area

For the calculation of the electrochemical surface area (ECSA) using eqn (2.5), several CVs were recorded within the potential range of ± 0.025 V *vs.* OCP at different scan rates, from 5 to 40 mV s^{-1}.

$$\text{ECSA} = \frac{C_{dl}}{C_s} \tag{2.5}$$

where C_{dl} is the double-layer capacitance calculated according to eqn (2.6), and C_s is the specific capacitance, whose value is 0.04 mF cm^{-2}.[51]

$$C_{dl} = \frac{\text{slope(upper)} + \text{slope(lower)}}{2} \tag{2.6}$$

where slope (upper) and slope (lower) are the slopes of the plot reporting the current recorded at the OCP *vs.* the scan rate; the former slope refers to the positive current at the OCP, whereas the latter refers to the negative current recorded at the OCP.

2.9. Density functional theory approach

Spin-polarized density functional theory (DFT) calculations were performed using the VASP package.[52–54] The Perdew–Burke–Ernzerhof (PBE) parametrization was employed for the exchange–correlation functional.[55] Projector Augmented Wave (PAW) pseudopotentials were used to describe core electrons,[56,57] and valence electrons were expanded with a plane wave, using a kinetic energy cutoff of 400 eV. Dispersion forces have been included by the Grimme's D3 scheme.[58] Geometry optimizations were performed by means of the conjugate gradient algorithm, with convergence criteria of electronic and ionic loops 10^{-5} eV and 10^{-2} eV A^{-1}, respectively. A 2 × 2 × 1 Monkhorst–Pack *k*-point grid[59] was used to sample the reciprocal space. To better capture the electronic structure of Fe centers and refine the electronic structure, single-point PBE0 (ref. 60) energy calculations were performed on PBE-optimized geometries. This strategy is a reliable compromise to avoid intense geometry optimizations with hybrid functionals, retaining accuracy.[61]

We started from the optimization of a graphene nanosheet and we created a $p(4 \times 4)$ supercell, with lattice parameters $a = b = 9.870$ Å, and $\gamma = 120°$.[62]

We created a carbon divacancy and built two different models: (i) a carbon divacancy and replaced with four atoms with nitrogen species; (ii) a carbon vacancy replacing the three undercoordinated carbon atoms with nitrogen atoms. The iron single atom was hosted in the cavity, leading to the formation of

FeN_4@Gr and FeN_3@Gr systems. In all cases, the atomic coordinates were fully relaxed. A vacuum layer of 15 Å was added to avoid spurious effects due to interaction between periodic replicas of the system.

Adsorption Gibbs free energies were calculated using the Computational Hydrogen Electrode (CHE) approach.[63,64] The Gibbs free energy ΔG_x of a given reaction intermediate x is obtained by adding entropic ΔS_x and zero-point energy $\Delta E_{zpe,x}$ contributions to the calculated DFT reaction energy, ΔE_x. Zero-point energies (ZPE) were calculated within the harmonic approximation by allowing the metal atoms and those of the intermediates to vibrate. Entropy of solid-state species was approximated from the vibrational partition function of the adsorbed intermediates,[65] whereas that of gas-phase species was taken from thermodynamic tables.

$$\Delta G_x = \Delta E_x - T\Delta S_x + \Delta E_{zpe,x}$$

In Section S2 are reported the working quantities, the cartesian coordinates and the structural parameters for the two single-site systems.

3. Results and discussion

3.1. Research design

This study presents a methodical investigation into the thermal stability and transformation of Fe–N_x active sites derived from FePc supported over carbon. The primary objective is to evaluate how the pyrolysis temperature, within a controlled range from RT to 600 °C, dictates the evolution of these sites and how these changes correlate with the electrochemical performance toward the NO_3RR in neutral pH.

To elucidate the evolutionary pathway of the Fe-moieties, specifically focusing on the atomically dispersed sites and their progressive structural evolution under thermal treatment, the fine structure of the iron K-edge was investigated *via ex situ* XAS at the SAMBA beamline. It was selected as the primary analytical tool due to its element-specific nature, providing unique insights into the electronic structure, local symmetry, and coordination environment of iron, even when present in small concentrations within a complex carbon matrix. The analysis focuses on both the X-ray Absorption Near-Edge Structure (XANES), which provides information on oxidation states and local coordination geometry, specifically monitoring the conversion from oxygen-adsorbed $(FePc)_2O$ species to planar Fe–N_x configurations, and the Extended X-ray Absorption Fine Structure (EXAFS), to quantify bonding characteristics and interatomic distances, including Fe–N, Fe–O, and the potential emergence of Fe–Fe bonds. These spectroscopic findings were integrated with complementary *ex situ* characterization techniques to obtain a comprehensive structural overview of the developed ECs.

3.2. Overall electrocatalysts characterization

The bulk structural properties and phase evolution of the synthesized samples were analysed *via* XRD and Raman Spectroscopy. The X-ray diffraction patterns, collected within the 2θ range of 5° to 80° (Fig. S1a), primarily exhibit the characteristic features of the carbonaceous support.

Two broad diffraction peaks at 2θ position of *ca.* 25° and 44° were indexed as (002) and (101) planes of carbon, respectively indicating defective and amorphous C.[66]

In the Fe_RT sample, the main characteristic reflections of β-FePc phase remain clearly detectable, and this confirms that the initial high-energy ball milling step physically blends the components while preserving the molecular integrity and long-range crystalline order of the precursor.

Upon pyrolysis, these molecular reflections disappear completely, and no new diffraction peaks corresponding to Fe-based crystalline species (such as metallic iron or iron oxides) emerge, even at the highest investigated temperature of 600 °C. This observation suggests a high degree of atomic dispersion within the carbon matrix, hindering the formation of large-scale clusters or crystalline aggregates. This is consistent with Muhyuddin *et al.* findings;[67] the lack of detectable oxide peaks does not necessarily imply the absence of such phases but rather indicates that any formed aggregates remain sub-nanometric in size or possess an amorphous structure that falls below the detection limit of conventional XRD.

Raman spectroscopy was employed to further investigate the carbonaceous framework of the synthesized ECs (Fig. S1b). While this method typically provides limited data regarding the iron-based active sites, the resulting spectra offer insights into the structural characteristics and degree of order within the carbon matrix. The spectra were comprised of characteristic 'D' and 'G' bands, located at 1330 cm^{-1} and 1590 cm^{-1}, respectively. The higher intensity of the D peaks in all ECs indicates the greater density of the structural defects in the carbon matrix. This observation is also consistent with the XRD outcomes showing the dominance of the defective and amorphous phase of carbon. The intensity ratio of the D to G band (I_D/I_G) can be used as an indicator for the estimation of defect density and degree of graphitization. For all the ECs, I_D/I_G came out to be higher than unity, *i.e.*, typically in the range of 1.48–1.54, which further endorses the higher degree of graphitic imperfections and disorders in carbon.

3.3. Morphological investigation

To provide direct evidence of the morphological evolution and elemental distribution of the iron species across the pyrolysis temperature range, BF-STEM coupled with EDX was performed (Fig. 1). For the samples pyrolyzed between RT and 400 °C, the BF-STEM images show a highly uniform distribution of iron, with no evidence of crystalline aggregates or large nanoparticles.

The corresponding EDX elemental maps for carbon, oxygen, and iron reveal that iron is homogeneously spread throughout the carbon matrix. The absence of detectable Fe clusters in these samples suggests that the metal centers remain atomically dispersed. A structural transition is observed starting at 500 °C, where the first sub-nanometric clustersbecome detectable. This process culminates at 600 °C with the formation of

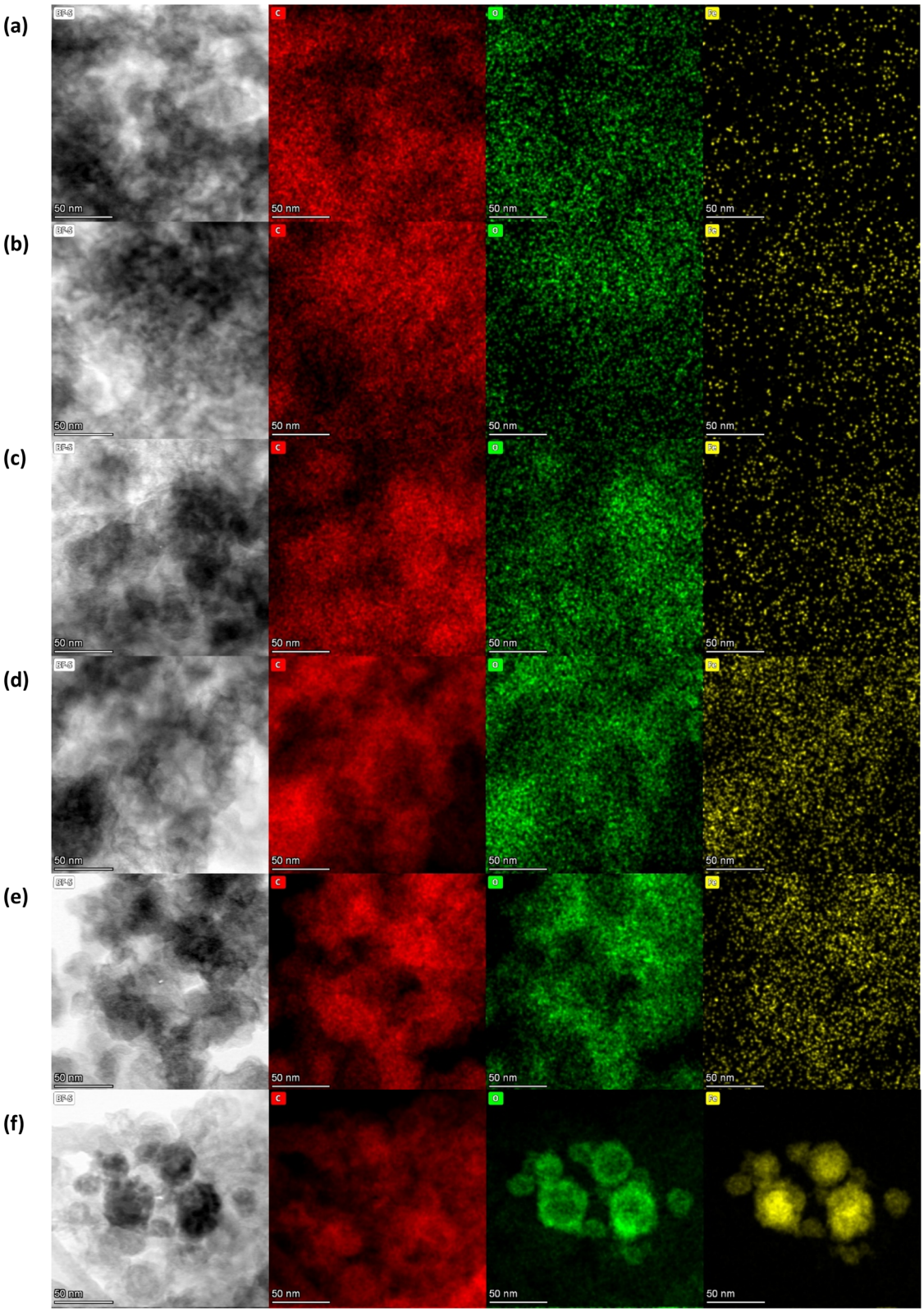

Fig. 1 STEM bright-field images and EDX of (a) Fe_RT, (b) Fe_200, (c) Fe_300, (d) Fe_400, (e) Fe_500 and (f) Fe_600. The first column shows the corresponding STEM bright-field images, whereas the second, third and fourth columns display the spatial distribution of carbon, oxygen and iron. All images are acquired at 530 K× magnifications.

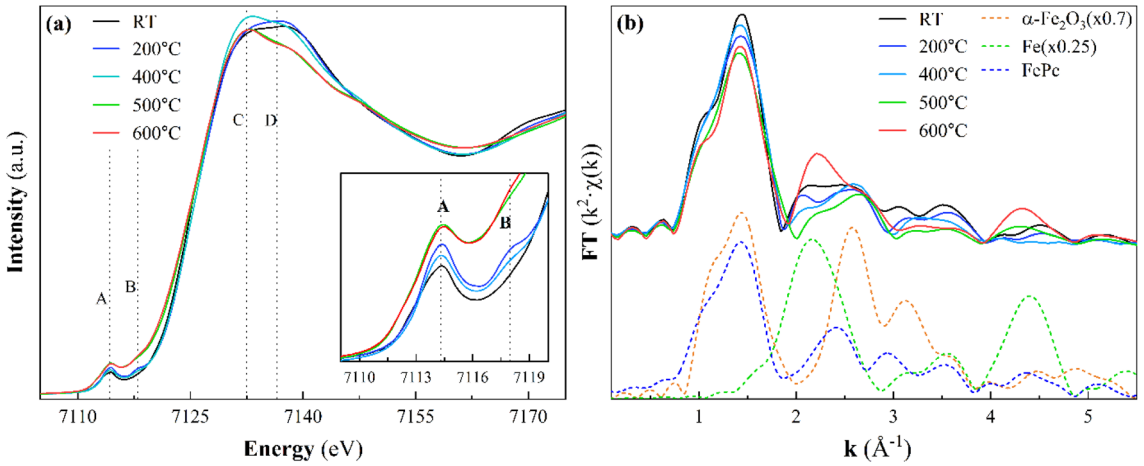

Fig. 2 (a) Normalized Fe K-edge XANES (with inset showing a magnified view on the pre-edge peak region); (b) k^2-weighted Fourier-Transformed EXAFS spectra of the different ECs. References spectra are shown as dashed lines, with intensity adjusted by a multiplication factor to improve visualization; FePc reference was retrived from XAFS DB portal.[68]

well-defined nanoparticles, visible as distinct dark contrasts in the BF-STEM images. EDX mapping of the Fe_600 sample confirms these aggregates as iron and oxygen-rich regions.

3.4. X-ray absorption spectroscopy through XANES and EXAFS analysis

The fine structure of the iron K-edge was investigated *via ex situ* XAS at the SAMBA beamline, focusing on both XANES and EXAFS. Normalized XANES spectra are shown in Fig. 2a.

The Fe_RT sample shows a typical FePc electronic structure, with an XANES composed of 4 features of interest. A pre-edge peak ~7114 eV is assigned to dipole-forbidden Fe 1s → 3d transitions. Its energy position relates to a ~Fe^{3+} oxidation state of the photoabsorbers,[49] while its intensity and broadening are expected for atomically dispersed Fe–N_4 sites. The observed symmetry suggests a tetragonal pyramidal (C_{4v}) geometry, likely due to oxygen adsorption forming $(FePc)_2O$.[50,69] Feature B, around 7118 eV, relates to dipole-allowed 1s → 4s transitions, typical of D_{4h} FePc symmetry.[50] The white line is further divided into components C and D, which relate to 1s → $4p_z$ and 1s → $4p_{x,y}$ transitions, respectively. Upon pyrolysis at 200 °C, moderate rises of the B and D features are observed, confirming the transition toward a planar D_{4h} symmetry due to oxygen desorption.[67] In agreement with theoretical simulations,[69] the relatively higher D feature suggests the prevalence of Fe–N_3 moieties in this stage. As the temperature increases from 400 °C to 600 °C, feature B persists, whereas we observe a relative increase in C and a gradual hindrance in D. From 500 °C, the decrease in white line intensity and the rise in the pre-edge region background suggest the formation of magnetite and/or metallic Fe nanoparticles. To quantify these structural transformations, Linear Combination Fitting (LCF) was performed. The initial reference dataset included all the species that were

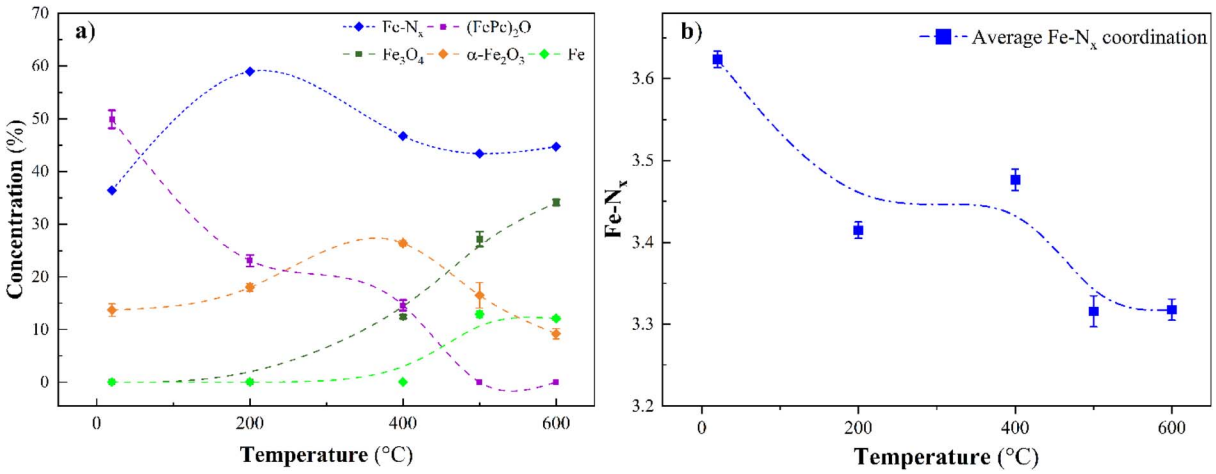

Fig. 3 (a) Species concentration estimated *via* LCF. The FeN_x comprend Fe–N_4 and FeN_3 references. (b) Average N coordination estimated from the relative concentration of Fe–N_4 (coordination 4), Fe–N_3 (3) and $(FePc)_2O$ (4). Errors are estimated as max variation between three fit iterations.

observe to form in previous works,[67,69] comprising several metallic and oxide Fe standards, and atomically dispersed Fe–N_x samples with different N coordination numbers. The dimensionality of the reference dataset was minimized *via* PCA and individual components were validated using the target transformation approach (details in Fig. S2–S5, Tables S1 and S2). In agreement with previous results,[67] this statistical approach confirmed the formation of three Fe-based metal/oxide side products along the temperature series, together with a modulation of the Fe–N_x local coordination as a function of the pyrolysis temperature.

Best fits (with 6 components) are shown in Fig. S5, while fitting results are listed in Table S2 and schematized in Fig. 3.

The results confirm the higher concentration of pyramidal $(FePc)_2O$ in the RT sample, as well as a ~14% concentration of hematite side product, which persists in the whole series of samples. At 200 °C, O adsorption is limited and while $(FePc)_2O$ concentration halves, tetragonal Fe–N_4 and especially Fe–N_3 concentration rises. At 400 °C, $(FePc)_2O$ content further decreases while magnetite appears (~12%) and becomes the preponderant side-product between 500 °C and 600 °C. Simultaneously, metallic Fe emerges at 500–600 °C, accounting for 12% of the total iron content. The LCF analysis suggests a gradual reduction of the Fe–N_x coordination as the temperature increases (Table S2).

EXAFS analysis provides deeper insights into the local coordination environment and the growth of iron-based nanoparticles. As shown in Fig. 2b, the EXAFS spectra of the RT sample confirm the structure expected from atomically dispersed Fe–N_x–C [67,69,70] with a relatively strong Fe–N scattering peak ~1.5 Å, and two extremely weak Fe–Fe (~2.1 Å) and Fe–C (2.6 Å) peaks.

Another component is observed around 1.1 Å, which can be assigned to Fe–O bonds in $(FePc)_2O$,[50,67] confirming the O absorption and $(FePc)_2O$ formation. Between 200 °C and 400 °C, a decrease in the intensity of both Fe–N and Fe–O peaks is observed, consistent with the conversion of $(FePc)_2O$ into Fe–N_x moieties.

As side product formation increases between 500 and 600 °C, we observe a further hindrance of the Fe–N intensity. In particular, at 600 °C, we observe the appearance of the Fe–Fe peak around 2.2 Å, as can be expected for metallic nanoparticle growth.

To better resolve the nature of the scattering atoms, Fig. 4 presents the wavelet-transformed Fe K-edge EXAFS spectra. This two-dimensional analysis offers enhanced resolution by

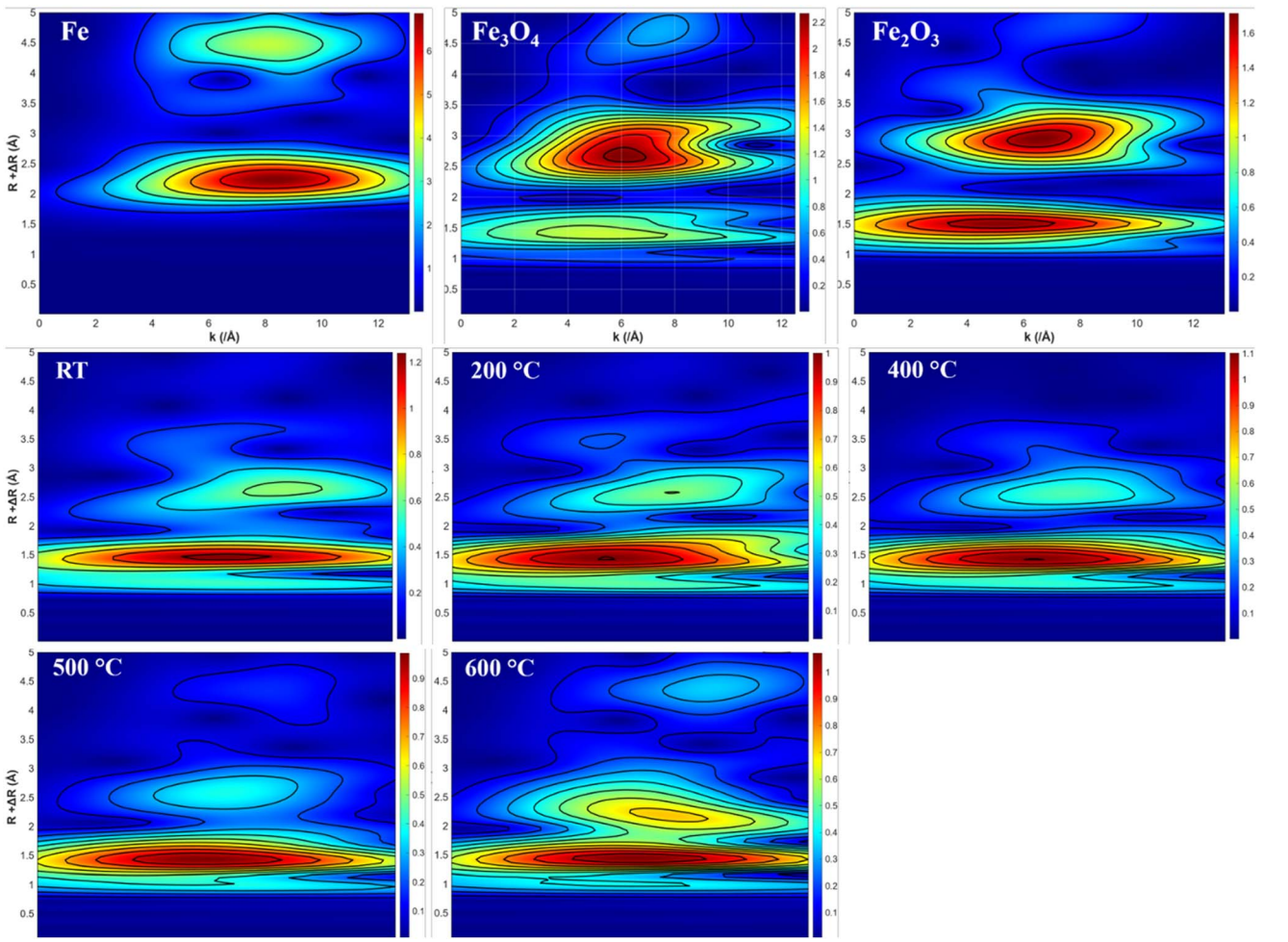

Fig. 4 k^3-Weighted wavelet-transformed Fe K-edge EXAFS spectra of references (first raw) and the different ECs (second and third raw).

simultaneously displaying the spatial and energy distributions of the neighbors surrounding the Fe center. The WT data corroborate the EXAFS discussion, clearly evidencing the emergence of a new Fe–Fe contribution centered around 2.2 Å at 600 °C. Interestingly, the XANES and EXAFS analyses reveal a discrepancy in the temperature at which nanoparticle growth begins. While XANES suggests a reduction of the metal centers starting at 500 °C, the characteristic Fe–Fe metallic peak only becomes evident in the EXAFS at 600 °C.

Considering the high sensitivity of XANES to oxidation state and the superior ability of EXAFS for coordination environment and aggregation, these results suggest that at 500 °C, the samples start to lose their N and C ligand coordination, resulting in the formation of reduced, yet isolated metallic Fe atoms, with no long-range order. At 600 °C, the appearance of the Fe–Fe peak requires the coalescence of Fe atoms into a nanoparticle and, hence, can be concluded to be the onset of nanoparticle formation.

3.5. Surface chemistry evaluation through XPS

The surface chemistry of the synthesized samples was investigated *via* XPS to evaluate the elemental composition and chemical speciation with the increase of the pyrolysis temperature. The results have been summarized respectively in Tables S3 and S4. The ECs are predominantly composed of carbon (>94 at%) with oxygen content generally below 4 at%, and nitrogen and iron levels below 3 at% and in average 0.3 ± 0.2 at%, respectively.

A notable exception is the Fe_500 sample, which exhibits a significantly higher oxygen content (~11 at%) and a lower carbon concentration (~87 at%). This oxygen enrichment at 500 °C aligns with the XAS findings, which indicated the maximum concentration of iron oxide phases (specifically magnetite) at this temperature before further reduction at higher thermal treatments.

Upon core levels deconvolution based on related literature, specific trends can be observed. The C 1s spectra (Fig. S6) were fitted with seven contributions: defective C (C def, <284 eV), graphitic C (C sp^2, 284.5 eV), C sp^3 contribution (~285 eV), C–O/C–N and C–O–C/C=N moieties between 285.5 and 287 eV, and higher oxidation states such as carbonyl and carboxyl groups (>287 eV).[71–75]

The carbon speciation remains largely homogeneous across the series, likely due to the stabilizing effect of the KJB support; graphitic content is maintained at approximately 60 rel.% for all samples, while the sp^3 contribution remains around 11 and 12 rel.%, with a slight increase to 14 rel.% for Fe_500.

Regarding N 1s speciation (Fig. S7), based on the phthalocyanine complex, three different nitrogen groups are considered: pyridinic N (~398.8 eV), nitrogen coordinated to Fe (N_x–Fe, 399.8 eV), and protonated/pyrrolic N (N–H, 400.5 eV).[76–79]

The N 1s profile is dominated by pyridinic and coordinating nitrogen atoms. Notably, for the samples treated at lower temperatures (RT, Fe_100, and Fe_200), the ratio between pyridinic and coordinating nitrogen is close to 1. As the temperature increases beyond 300 °C, the relative content of pyridinic N rises to 70 rel.%, while the Fe–N_x moiety gradually decreases. Finally, in the Fe 2p spectra (Fig. S8), two major contributions are assigned to a main N-coordinated Fe(II) (Fe–N_x/Fe(II), 709–710 eV) and Fe(III) species (711–712 eV)[80–83] with their respective characteristic satellites at 715–716 eV and 718–720 eV.[84,85]

In the set 200–600, the FePc complex stabilizes a vast majority (~60 rel.%) of N-coordinated metal possessing an oxidation number of +2. Such a configuration is maintained stable among the samples, as per Fe(III) content. Overall, characteristic satellite peaks are observed for Fe(II) and Fe(III) ascribed to Fe in high-spin configurations.[84,85]

3.6. Electrochemical performance towards NO_3RR

As a fundamental study, this work focused on neutral pH (pH 6.3) to evaluate the electrocatalytic activity of the different ECs toward the NO_3RR.

For each EC, LSVs were recorded both in 0.1 M PBS and in 0.1 M PBS + 0.16 M NO_3^- to have a first evaluation of HER and NO_3RR activity, respectively. The onset potential was defined as the potential at which the current density reached −0.4 mA

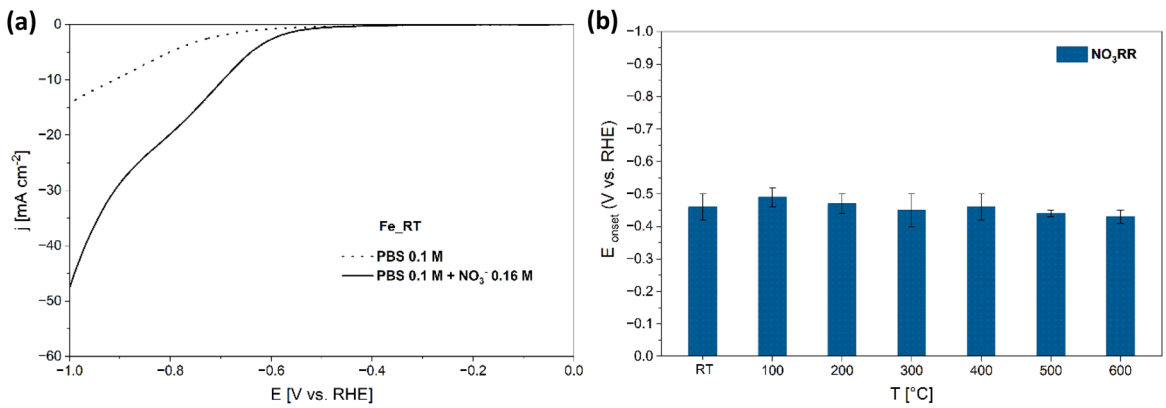

Fig. 5 (a) Representative LSV curves for the Fe_RT EC in 0.1 M PBS (dotted line), and in 0.1 M PBS + 0.16 M NO_3^- (solid line). Complete LSV profiles for all tested electrocatalysts are provided in Fig. S9. (b) Onset potentials for NO_3RR derived from the LSV data, defined as the potential at which a current density of −0.4 mA cm^{-2} is reached.

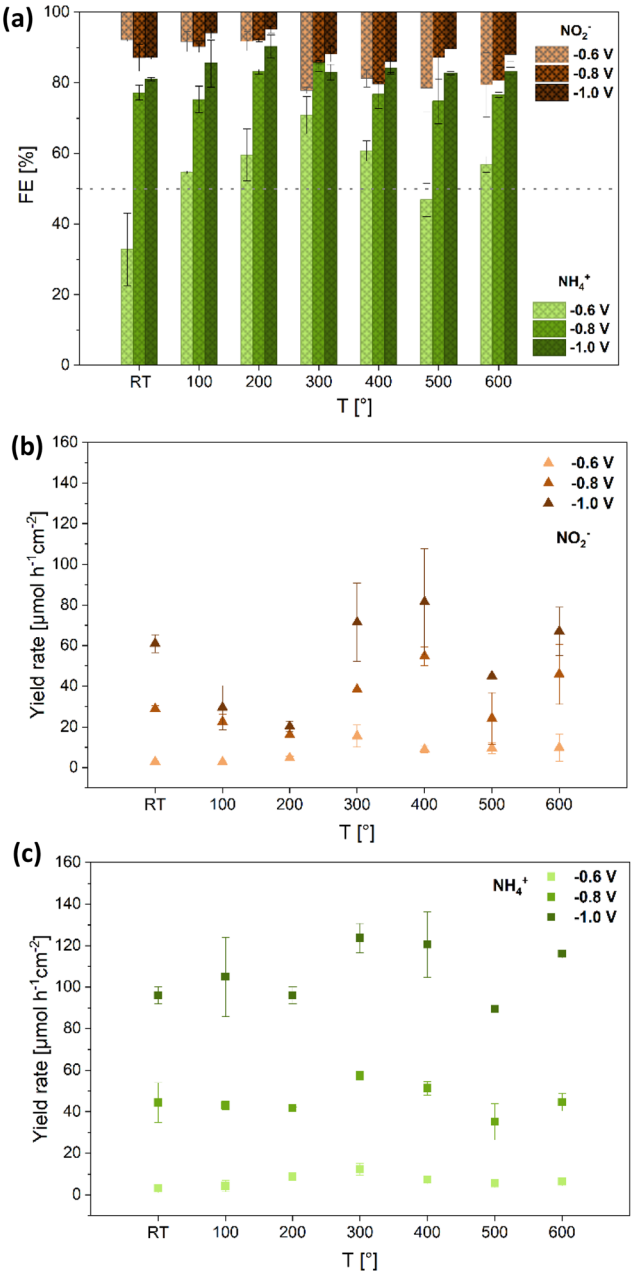

Fig. 6 Gap analysis plot (GAP) for the electrochemical NO_3RR for all ECs in 0.1 M PBS + 0.16 M NO_3^- for 1 h. (a) Faradaic efficiency for NO_2^- (orange; top-down) and NH_4^+ (green; bottom-up) at −0.6 V, −0.8 V and −1.0 V *vs.* RHE. A horizontal line is set at 50% FE to guide the eye. The bottom section of the figure shows the corresponding yield rate (µmol h^{-1} cm^{-2}) for (b) NO_2^- (orange, triangle) and (c) NH_4^+ (green, square) as a function of the applied potentials. A simplified plot is reported in Fig. S15 and S16, whereas the data are presented in Tables S6 and S7.

cm^{-2}, enabling consistent comparison across materials.[18] The corresponding potential values at −0.4 mA cm^{-2} extracted from these LSVs are summarized in Table S5.

As shown in Fig. 5a, the Fe_RT sample, even without thermal treatment, presents a good electrocatalytic response in the presence of nitrate, with current densities reaching approximately 50 mA cm^{-2} at −1 V *vs.* RHE. In contrast, the current density in PBS alone remains around 10 mA cm^{-2} at the same potential, confirming high specificity for NO_3RR and minimal HER interference.

Notably, this significant difference between the current recorded in pure PBS and in the nitrate-containing electrolyte was consistently observed across the entire series of electrocatalysts, as shown in the complete LSV profiles (Fig. S9), underscoring the general selectivity of these materials toward nitrate reduction.

However, because the differences in the recorded onset potentials among the various samples appear marginal (Fig. 5b), these polarization curves provide only a preliminary indication of selectivity, making a long-term potentiostatic investigation necessary to rigorously differentiate the catalytic responses.

To investigate the NO_3RR activity and selectivity of the different materials towards NH_4^+ and NO_2^-, a series of one hour potential holds were performed at −0.6 V, −0.8 V, and −1.0 V *vs.* RHE in 0.1 M PBS + 0.16 M NO_3^- (Fig. 6). The corresponding current–time profiles are shown in Fig. S10.

Since the primary scope of this work is focused on structure–property correlations rather than an exhaustive mechanistic or kinetic investigation, the quantification of other eventual trace intermediates (such as NH_2OH and NO) was not targeted.

The quantitative peaks for both NH_4^+ and NO_2^-, along with their corresponding calibration curves for cation and anion analyses, are reported in Fig. S11–S13.

First, to establish the background activity of the substrate, CA tests were conducted on bare carbon paper and on carbon paper coated with electrocatalyst-free ink.

IC analysis of the electrolyte after these one-hour tests revealed negligible amounts of NO_2^- and NH_4^+, confirming the absence of significant nitrate reduction from the carbon paper, the ionomer and the Aquivion membrane.

Nevertheless, since the nitrogen in the catalysts could act as a contamination source, CA tests were also performed in a pure 0.1 M PBS electrolyte (without NO_3^-) at highly reducing potentials. Also in this case, there was no detectable formation of NH_4^+ or NO_2^-, confirming that the coordinated nitrogen in the carbon matrix is electrochemically stable and doesn't convert into ammonia.

Finally, as a crucial control experiment, the bare carbon support (KJB) was evaluated under identical reaction conditions (Fig. S14). It exhibited low current densities, and, even though the production of both NH_4^+ and NO_2^- was observed, the resulting FEs and yield rates were suppressed across all investigated potentials compared to the Fe-containing samples.

The FE and yield rate for ammonia production show a marked dependence on both the applied potential and the pyrolysis temperature (Table S6).

At the lowest overpotential investigated (−0.6 V *vs.* RHE) the Fe_RT sample exhibits the lowest performance, with an FE of 32.9% and a yield rate of ∼3 µmol h^{-1} cm^{-2}. This behavior is further supported by the LSV analysis seen previously, where Fe_RT displayed the most negative onset potential. Thermal treatment leads to a progressive increase in ammonia production:

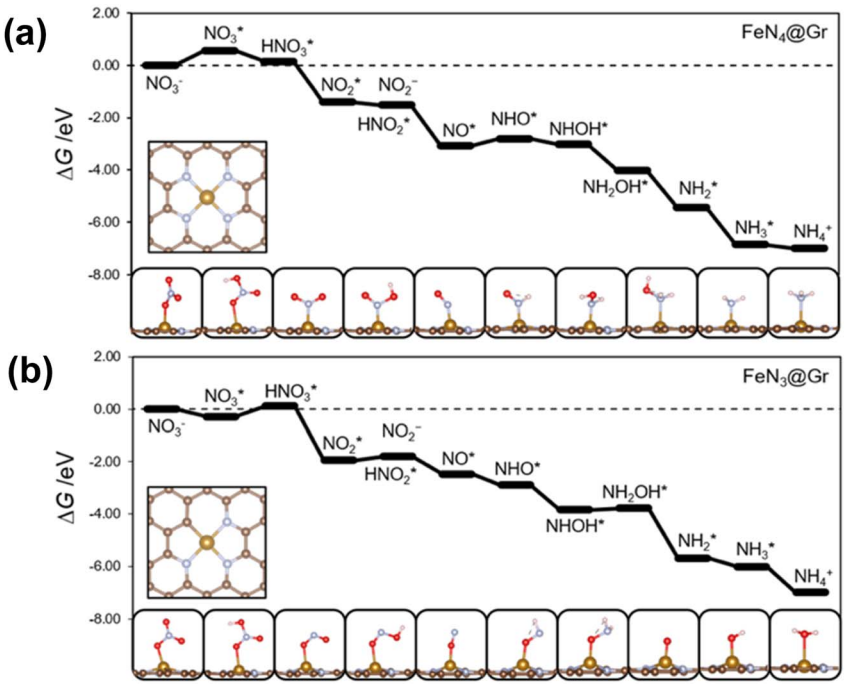

Fig. 7 Gibbs free energy profile of NO_3RR for (a) FeN_4@Gr and (b) FeN_3@Gr. In the insets are shown the structures of active site model and adsorbed intermediates.

the Fe_300 sample reaches the maximum value for this potential, with an FE of 70.1% and a yield rate of 12.3 μmol h^{-1} cm^{-2}.

At more cathodic potentials (−0.8 V and −1.0 V *vs.* RHE), the differences in FE between the ECs become less pronounced, as all materials surpass 74% efficiency. At −0.8 V *vs.* RHE, the FE values range from 74.9% (Fe_500) to 85.4% (Fe_300). At −1.0 V, the FE further stabilizes between 80% and 90% across the entire series.

However, the yield rates exhibit a significant increase at this potential; Fe_300 and Fe_400 record the highest production levels, reaching 123.7 and 120.5 μmol h^{-1} cm^{-2}, respectively.

The selectivity of the ECs was further assessed by quantifying the partial reduction of NO_3^- to NO_2^- (Table S7).

Across all tested potentials, the FE for NO_2^- remains significantly lower than that for NH_4^+, confirming that NH_4^+ is the primary product of the reaction for all the materials. As the applied potential decreases, the yield rates increase alongside the total current while the FE follows a generally opposite trend. In fact, for most ECs, the FE at −1.0 V *vs.* RHE is lower than the values recorded at −0.8 or −0.6 V *vs.* RHE. For instance, in the Fe_300 sample, the FE drops from ∼22% at −0.6 V to ∼12 at −1.0 V *vs.* RHE.

These results indicate that at high overpotentials, the 8 e^- reduction path toward ammonia is kinetically favored over the 2-e^- partial reduction to nitrite, leading to a higher overall selectivity for the final product.

Only experimentally quantified products *via* IC are displayed in the Gap Analysis Plot (GAP) in Fig. 6a, while the unquantified HER fraction and possible traces of nitrogenous compounds (N_2H_2, N_2 and NO_x) constitute the remaining balance.

However, since H_2 is considered the primary byproduct, the remaining fraction of the total charge not accounted for by NH_4^+ and NO_2^- production is attributed to the competitive HER.

The impact of HER is most prominent at lower overpotentials and for the untreated sample. In fact, at −0.6 V *vs.* RHE, the Fe_RT catalyst shows a combined FE ($NH_4^+ + NO_2^-$) of only ∼41%, suggesting that ∼59% of the electrons are consumed by the HER.

In contrast, thermal treatment significantly suppresses water reduction in favor of nitrate activation; at the same potential, the total FE for NO_3RR products in the Fe_300 sample reaches approximately 93%, indicating a minimal contribution from the HER.

As the potential shifts to −0.8 V and −1.0 V *vs.* RHE, the cumulative FE for all materials consistently stabilizes above 90–95%. This high recovery of the total charge demonstrates that at these overpotentials, the NO_3RR kinetics effectively outcompeted HER, regardless of the specific structural evolution of the iron sites.

To investigate the variation of the accessible interface, the double-layer capacitance (C_{dl}) and the electrochemically active surface area (ECSA) were systematically quantified (Fig. S17 and Table S8). The ECSA remains remarkably stable and comparable within the RT-400 °C range (fluctuating between 80 and 90 m^2 g^{-1}). This conservation allows us to exclude electrochemical surface area variation as the driving factor for the electrochemical performances differences in this window.

Conversely, the ECSA significantly drops to approximately 60 m^2 g^{-1} at 600 °C.

The reason of this contraction could be the thermal coalescence of atomically dispersed Fe into larger nanoparticles that leads to a substantial loss of the exposed catalytic surface.

In Table S9, all the operating conditions and the results achieved by different Fe–N_x–C EC for NO_3RR in previous studies have been summarized; Fe_300 has been considered as representative material for this work.

3.7. Computational section

The NO_3RR reaction pathway is extremely complex as it can pass through a large spectrum of possible intermediates. We made sure to trace the most stable reaction path, which is comprised of the most stable reaction intermediates within *ab initio* thermodynamics. In particular, we simulated the possible adsorption configurations for each reaction step and selected the most stable intermediate. Then, we started from the most stable intermediate and we simulated all possible adsorption configurations of the subsequent step, taking the most stable intermediate. The procedure was iterated for all electrochemical steps of the reaction. This strategy was adopted in previous studies for the computational study of nitrogen reduction reaction.[86,87] The first step of the reaction, nitrate adsorption, has been evaluated adopting the methodology proposed by Calle-Vallejo and coworkers.[88]

We considered the following elementary steps:

$$(1)\ * + NO_3^- \rightarrow NO_3^* + e^-$$

$$(2)\ NO_3^* + H^+ + e^- \rightarrow NO_3H^*$$

$$(3)\ NO_3H^* + H^+ + e^- \rightarrow NO_2^* + H_2O$$

$$(4)\ NO_2^* + H^+ + e^- \rightarrow NO_2H^*$$

$$(5)\ NO_2H^* + H^+ + e^- \rightarrow NO^* + H_2O$$

$$(6)\ NO^* + H^+ + e^- \rightarrow NOH^*$$

$$(7)\ NOH^* + H^+ + e^- \rightarrow NHOH^*$$

$$(8)\ NOH^* + H^+ + e^- \rightarrow NH_2O^*$$

$$(9)\ NOH^* + H^+ + e^- \rightarrow N^* + H_2O$$

$$(10)\ NHOH^* + H^+ + e^- \rightarrow NH_2OH^*$$

$$(11)\ NHOH^* + H^+ + e^- \rightarrow NH^* + H_2O$$

$$(12)\ NH_2O^* + H^+ + e^- \rightarrow O^* + NH_3$$

$$(13)\ N^* + H^+ + e^- \rightarrow NH^*$$

$$(14)\ NH_2OH^* + H^+ + e^- \rightarrow NH_2^* + H_2O$$

$$(15)\ NH^* + H^+ + e^- \rightarrow NH_2^*$$

$$(16)\ O^* + H^+ + e^- \rightarrow OH^*$$

$$(17)\ NH_2^* + H^+ + e^- \rightarrow NH_3^*$$

$$(18)\ OH^* + H^+\ e^- \rightarrow H_2O^*$$

$$(19)\ NH_3^* + H^+ \rightarrow NH_4^+ + *$$

$$(20)\ H_2O^* \rightarrow H_2O + *$$

Experimental evidence reports a Fe–N coordination number ranging from about four to three. For this reason, we performed the *ab initio* thermodynamics analysis for FeN_4 and FeN_3 active sites.

We created a carbon divacancy and built two different models: (i) all four undercoordinated carbon atoms were replaced with nitrogen species; (ii) the three undercoordinated carbon atoms where replace with nitrogen atoms. The iron single atom was hosted in the available cavity, leading to the formation of FeN_4@Gr and FeN_3@Gr systems. Previous works suggested that even such subtle changes can alter significantly the reactivity.[89]

The two free energy profiles show different preferred pathways (Fig. 7). In particular, the profile of FeN_4 involves stabilisation of the reaction intermediates by Fe–O bonding, whereas the pathway on FeN_3 involves the binding of the Fe atom to an N atom.

The FeN_3 system exhibits a smaller thermodynamic barrier of 0.40 eV, corresponding to the $NO_3^* \rightarrow NO_3H^*$ elementary step, whereas the FeN_4 system exhibits a barrier of 0.56 eV, corresponding to NO_3^- adsorption.

The symmetry breaking from Fe–N_4 to Fe–N_3, where iron-nitrogen coordination changes from fourfold square planar, to trigonal, induces an increase in reactivity of the catalyst. A similar behaviour has been observed also in a previous work on carbon dioxide electroreduction.[89] Indeed, a subtle structural difference between FeN_4 and FeN_3 active sites results in significant modifications to their electronic properties. In particular, FeN_3 has a higher electronic density of states near the Fermi level with respect to FeN_4 (Fig. S23), suggesting that more electronic states are available to participate in charge transfer during the adsorption.

This enhanced electronic availability is further supported by Bader charge analysis.[90–93] Upon NO_3^- adsorption, which

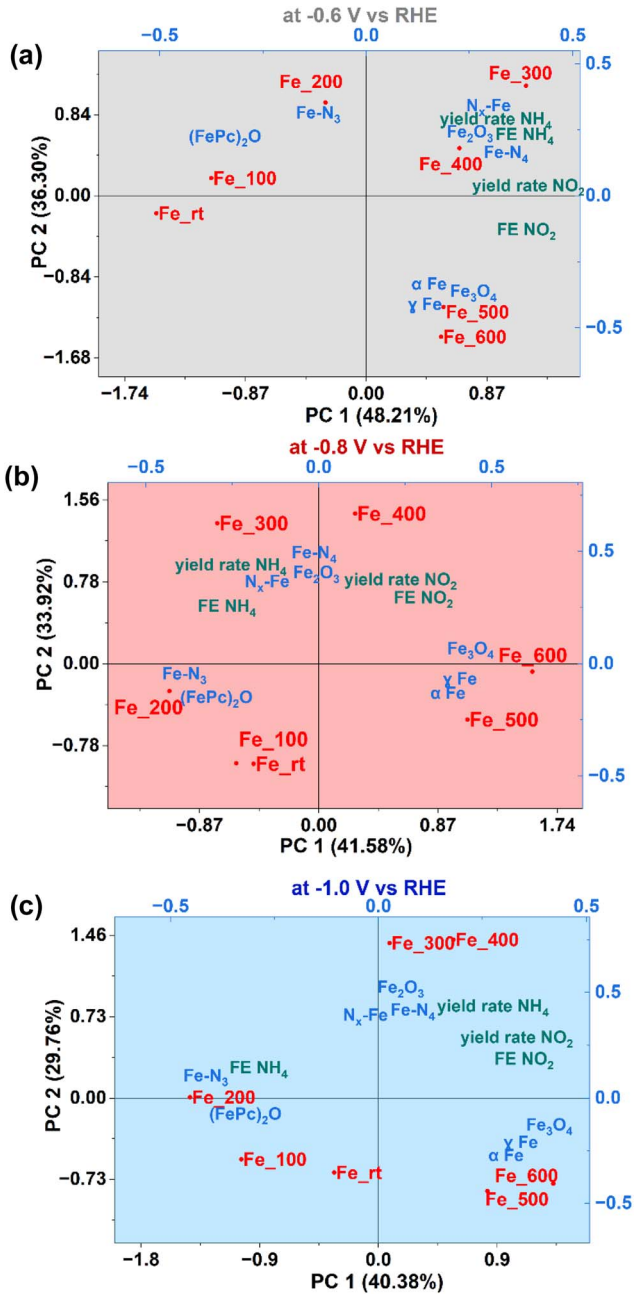

Fig. 8 Principal component analysis (PCA) obtained at (a) −0.6 V, (b) −0.8 V and (c) −1.0 V *vs.* RHE.

constitutes the rate-determining step of the NO_3RR on FeN_4, the charge transfer to the Fe center in the FeN_3 site is greater that in the FeN_4 site, with changes of the atomic charge of the metal center of 0.3 e and 0.1 e, respectively.

3.8. Structure-to-property relationships

To unravel the correlations between the structural evolution of the iron sites and the electrochemical performance in the NO_3RR, a Principal Component Analysis (PCA) was performed by integrating structural and performance descriptors obtained at three different applied potentials.

This multivariable approach allowed for the combination of descriptors derived from XPS, such as the total N_x–Fe content derived from N1s spectra, and those obtained from XANES, including the relative fractions of Fe–N_3, Fe–N_4, $(FePc)_2O$, metallic and oxide phases, correlating them directly with the yield rate and FE for NH_4^+ and NO_2^- (Fig. 8).

The PCA models remain statistically representative across all conditions, with the first two principal components explaining 81.49%, 72.74%, and 67.10% of the total variance at −0.6 V, −0.8 V, and −1.0 V *vs.* RHE, respectively.

At low overpotential (−0.6 V *vs.* RHE), both the yield rate and FE for NH_4^+ are strongly correlated with the total density of coordinated sites (N_x–Fe) and, specifically, with the presence of the Fe–N_4 species. This behavior is exemplified by the samples pyrolyzed at 300 °C and 400 °C, which cluster in the high-performance quadrant of the PCA plot. A similar trend is observed at −0.8 V *vs.* RHE.

However, while the yield rate remains associated with the Fe–N_x descriptors, the FE begins to diverge, initiating a rotation toward the Fe–N_3 species. This shift culminates at −1.0 V *vs.* RHE, where the FE NH_4^+ vector aligns directly with the Fe–N_3 descriptor and moves closer to the sample pyrolyzed at 200 °C. This suggests that the trigonal geometry of the Fe–N_3 site becomes the determining factor for maintaining high FE at high overpotentials, when the competition with the competitive HER increases.

These experimental and statistical findings are in excellent agreement with our computational analysis and recent literature. Specifically, Liu *et al.*[94] systematically compared the catalytic behavior of Fe–N_4, Fe–N_3, and Fe–N_4–OH active sites. Through a combination of *operando* attenuated total reflection surface-enhanced infrared absorption spectroscopy (ATR-SEIRAS) and DFT calculations, they demonstrated that the highest NO_3RR activity is associated with Fe–N_3 coordination.

This phenomenon conceptually aligns also with broader conceptual frameworks established for SACs in electrochemical nitrogen fixation.

In particular, studies conducted on non-carbonaceous matrices, have demonstrated that fine-tuning the peripheral electronic environment and charge transfer efficiency can successfully overcome major thermodynamic bottlenecks in multi-proton/electron configurations.[95]

In these systems, an orbital "acceptance-donation" orbital mechanism controls the adsorption of nitrogenous species, altering intermediate scaling relationships and suppressing competitive HER.

The impact of higher thermal treatments emerges clearly from the analysis of the samples at 500 °C and 600 °C, which systematically occupy quadrants opposite to the ammonium performance vectors throughout the tested potential range. The statistical segregation of these materials is closely linked to their association with iron phases, such as Fe_3O_4 and metallic iron in the α and γ forms. Such evidence confirms that the loss of atomic dispersion and the growth of nanoparticles, detected in both EXAFS and STEM analyses, negatively affect the NO_3RR toward the desired final product.

Finally, the temperature-dependent evolution of each species is detailed in Fig. S18, while the linear correlations between the relative abundance of the structural variables and the performance metrics are illustrated in Fig. S19–S22.

Despite the inherent complexity of the system and the scattering observed for some data points, a clear trend emerges: the FE and yield rate of NH_4^+ significantly increase with the percentage of total Fe–N_x and Fe–N_4 sites. This dependence is particularly evident at lower overpotentials, further validating the PCA findings.

4. Conclusions

This work presents a detailed investigation into the structural evolution and electrocatalytic performance of Fe–N_x electrocatalysts (ECs) derived from iron phthalocyanine (FePc) for the nitrate reduction reaction (NO_3RR). Commercial conductive carbon black (Ketjenblack EC-600JD) was functionalized with 20 wt% FePc and underwent pyrolysis across a temperature range from RT to 600 °C in N_2/H_2 atmosphere. Through a combination of advanced microscopic and spectroscopic techniques, the evolution, growth and transformation of active moieties were elucidated, establishing a structure–property relationship by testing the NO_3RR response of the samples in neutral pH electrolytes.

The findings demonstrate that the pyrolysis temperature dictates the coordination environment and dispersion of the iron centers. The thermal treatments promote the conversion of molecular $(FePc)_2O$ into atomically dispersed Fe–N_x moieties, predominantly Fe–N_4 and Fe–N_3, which eventually aggregate in nanoparticles at 600 °C. Within this structural evolution, the EC pyrolyzed at 300 °C, exhibited the best NO_3RR activity, although the faradaic efficiency (FE) for ammonia remains consistently above 75% at −0.8 V *vs.* RHE for all samples.

To fully understand these experimental results, Principal Component Analysis (PCA) was employed to decouple the contributions of different iron species. The statistical model revealed that while the total density of Fe–N_x and Fe–N_4 sites governs the reaction rate at low overpotentials, the specific presence of the trigonal Fe–N_3 configuration is the key descriptor for maintaining high FE at high overpotentials. Conversely, the emergence of metallic clusters at 500–600 °C was statistically correlated with a decrease in the catalytic selectivity. These experimental and statistical findings were corroborated by quantum chemical simulations, which confirmed that the Fe–N_3 site is intrinsically more active than the planar Fe–N_4 geometry. In particular, the Fe–N_3 active site exhibits a smaller thermodynamic barrier (0.40 eV) for the $NO_3^* \rightarrow NO_3H^*$ elementary step, compared to the Fe–N_4 system (0.56 eV for NO_3^- adsorption).

Overall, this study provides fundamental insights into the structure–activity relationships of single-atom Fe–N_x–C ECs derived from FePc for the NO_3RR.

Conflicts of interest

The authors declare that they have no conflict of interest.

Data availability

The data supporting this article have been included as part of supplementary information (SI). Supplementary information: XRD pattern, Raman spectra, Principal Component Analysis (PCA) of the Fe K-edge XANES dataset, linear combination fit of the Fe spectra, elemental composition and chemical speciation of the different ECs determined by XPS, electrochemical data including onset potential determination, linear sweep voltammetry and chronoamperometry, IC calibration and quantification for nitrate, nitrite and ammonia, activity and selectivity of the materials identifying faradaic efficiency and yield rate, correlations between activity and selectivity and DFT calculations. See DOI: https://doi.org/10.1039/d6ta04062d.

Acknowledgements

C. S. would like to acknowledge the European Union – NextGeneration EU from the Italian Ministry of Environment and Energy Security POR H2 AdP MMES/ENEA with involvement of CNR and RSE, PNRR – Mission 2, Component 2, Investment 3.5 "Ricerca e sviluppo sull'idrogeno" under the ENEA – UNIMIB agreement (Procedure 1.1.3 PNRR POR H2). The authors thank Synchrotron SOLEIL for provision of the beam at the SAMBA beamline.

References

1 V. Pattabathula and J. Richardson, Introduction to Ammonia Production, *Chem. Eng. Prog.*, 2016, **112**, 69–75.
2 C. Egenhofer, L. Schrefler, V. Rizos, *et al.*, *The Composition and Drivers of Energy Prices and Costs in Energy-Intensive Industries: The Case of Ceramics, Glass and Chemicals*, CEPS Special Report, 2014, vol. 85.
3 M. Muhyuddin, G. Zuccante, P. Mustarelli, *et al.*, Electrochemical urea production using carbon dioxide and nitrate: state of the art and perspectives, *Energy Environ. Sci.*, 2024, **17**, 3739–3752.
4 L. R. Winter and J. G. Chen, N_2 Fixation by Plasma-Activated Processes, *Joule*, 2021, **5**, 300–315.
5 H. S. Ahmed, Z. Yahya, W. Ali khan, *et al.*, Sustainable pathways to ammonia: a comprehensive review of green production approaches, *Clean Energy*, 2024, **8**, 60–72.
6 Y. Ren, C. Yu, X. Tan, *et al.*, Strategies to suppress hydrogen evolution for highly selective electrocatalytic nitrogen reduction: Challenges and perspectives, *Energy Environ. Sci.*, 2021, **14**, 1176–1193.
7 C. J. M. Van der Ham, M. T. M. Koper and D. G. H. Hetterscheid, Challenges in reduction of dinitrogen by proton and electron transfer, *Chem. Soc. Rev.*, 2014, **43**, 5183–5191.
8 D. Hao, Z. G. Chen, M. Figiela, *et al.*, Emerging alternative for artificial ammonia synthesis through catalytic nitrate reduction, *J. Mater. Sci. Technol.*, 2021, **77**, 163–168.
9 Z. Y. Wu, M. Karamad, X. Yong, *et al.*, Electrochemical ammonia synthesis *via* nitrate reduction on Fe single atom catalyst, *Nat. Commun.*, 2021, **12**, 2870.

10 S. Lombardi, T. Rodriguez-Flores, G. Prina, *et al.*, Comparative Study of Cobalt, Copper and Zinc Oxides for the Electrochemical Reduction of Nitrate to Ammonia, *Electrochim. Acta*, 2025, **548**, 147870.
11 C. Wang, Y. Zang, H. Luo, *et al.*, Iron-Based Nanocatalysts for Electrochemical Nitrate Reduction, *Small Methods*, 2022, **6**, 2200790.
12 E. Murphy, Y. Liu, I. Matanović, *et al.*, Highly Durable and Selective Fe- and Mo-Based Atomically Dispersed Electrocatalysts for Nitrate Reduction to Ammonia *via* Distinct and Synergized NO_2- Pathways, *ACS Catal.*, 2022, **12**, 6651–6662.
13 T. Zhang, D. Zhang, X. Han, *et al.*, Preassembly Strategy to Fabricate Porous Hollow Carbonitride Spheres Inlaid with Single Cu-N_3 Sites for Selective Oxidation of Benzene to Phenol, *J. Am. Chem. Soc.*, 2018, **140**, 16936–16940.
14 Z. Jin, P. Li, Y. Meng, *et al.*, Understanding the inter-site distance effect in single-atom catalysts for oxygen electroreduction, *Nat. Catal.*, 2021, **4**, 615–622.
15 S. Rojas-Carbonell, C. Santoro, A. Serov, *et al.*, Transition metal-nitrogen-carbon catalysts for oxygen reduction reaction in neutral electrolyte, *Electrochem. Commun.*, 2017, **75**, 38–42.
16 T. Asset, S. T. Garcia, S. Herrera, *et al.*, Investigating the Nature of the Active Sites for the CO_2 Reduction Reaction on Carbon-Based Electrocatalysts, *ACS Catal.*, 2019, **9**, 7668–7678.
17 W. Ju, A. Bagger, G. P. Hao, *et al.*, Understanding activity and selectivity of metal-nitrogen-doped carbon catalysts for electrochemical reduction of CO_2, *Nat. Commun.*, 2017, **8**, 944.
18 E. Murphy, Y. Liu, I. Matanović, *et al.*, Elucidating electrochemical nitrate and nitrite reduction over atomically-dispersed transition metal sites, *Nat. Commun.*, 2023, **14**, 4843.
19 T. Sun, W. Zang, J. Sun, *et al.*, SACs on Non-Carbon Substrates: Can They Outperform for Water Splitting?, *Adv. Funct. Mater.*, 2023, **33**, 2301526.
20 W. Yang, J. Wang, R. Chen, *et al.*, Reaction mechanism and selectivity regulation of photocatalytic nitrate reduction for wastewater purification: progress and challenges, *J. Mater. Chem. A*, 2022, **10**, 17357–17376.
21 R. Li, T. Gao, P. Whang, *et al.*, The origin of selective nitrate-to-ammonia electroreduction on metal-free nitrogen-doped carbon aerogel catalysts, *Appl. Catal., B*, 2023, **331**, 122708.
22 Z. W. Seh, J. Kibsgaard, C. F. Dickens, *et al.*, Combining theory and experiment in electrocatalysis: Insights into materials design, *Science*, 2017, **355**, eaad4998.
23 Q. Song, M. Li, X. Hou, *et al.*, Fe atoms for N=O bond activation to boost electrocatalytic nitrate reduction at low concentrations, *Appl. Catal., B*, 2022, **317**, 121734.
24 P. Li, Z. Jin, Z. Fang, *et al.*, A single-site iron catalyst with preoccupied active centers that achieves selective ammonia electrosynthesis from nitrate, *Energy Environ. Sci.*, 2021, **14**, 3522–3531.
25 T. Asset and P. Atanassov, Iron-nitrogen-carbon catalysts for proton exchange membrane fuel cells, *Joule*, 2020, **4**, 33–44.
26 M. Muhyuddin, E. Beretti, C. Roiron, *et al.*, Atomically Dispersed Electrocatalysts for Oxygen Reduction Reaction: Understanding the Synthetic Processes for Tuning Structure, Surface Chemistry, and Formation of Different Active Sites, *ACS Appl. Energy Mater.*, 2025, **8**, 6845–6856.
27 S. Rojas-Carbonell, K. Artyushkova, A. Serov, *et al*, Effect of pH on the Activity of Platinum Group Metal-Free Catalysts in Oxygen Reduction Reaction, *ACS Catal.*, 2018, **8**, 3041–3053.
28 A. Cosenza, L. Delafontaine, A. Ly, *et al.*, Novel acid-free process intensification for the synthesis of non-precious metal-nitrogen-carbon electrocatalysts for oxygen reduction reaction, *J. Power Sources*, 2023, **556**, 232382.
29 A. Serov, M. H. Robson, M. Smolnik, *et al.*, Tri-metallic transition metal–nitrogen–carbon catalysts derived by sacrificial support method synthesis, *Electrochim. Acta*, 2013, **109**, 433–439.
30 S. Mostoni, L. Mirizzi, A. Frigerio, *et al.*, In-Situ HF Forming Agents for Sustainable Manufacturing of Iron-Based Oxygen Reduction Reaction Electrocatalysis Synthesized Through Sacrificial Support Method, *ChemSusChem*, 2025, **18**, e202401185.
31 C. Santoro, A. Serov, K. Artyushkovaet, *et al.*, Platinum group metal-free oxygen reduction electrocatalysts used in neutral electrolytes for bioelectrochemical reactor applications, *Curr. Opin. Electrochem.*, 2020, **23**, 106–113.
32 A. Serov, M. H. Robson, B. Halevi, *et al.*, Highly active and durable templated non-PGM cathode catalysts derived from iron and aminoantipyrine, *Electrochem. Commun.*, 2012, **22**, 53–56.
33 M. Kodali, R. Gokhale, C. Santoro, *et al.*, High performance platinum group metal-free cathode catalysts for microbial fuel cell (MFC), *J. Electrochem. Soc.*, 2017, **164**, H3041–H3046.
34 M. H. Robson, A. Serov, K. Artyushkova, *et al.*, A mechanistic study of 4-aminoantipyrine and iron derived non-platinum group metal catalyst on the oxygen reduction reaction, *Electrochim. Acta*, 2013, **90**, 656–665.
35 Z. Meng, N. Chen, S. Cai, *et al.*, Rational design of hierarchically porous Fe-N-doped carbon as efficient electrocatalyst for oxygen reduction reaction and Zn-air batteries, *Nano Res.*, 2021, **14**, 4768–4775.
36 Y. Mun, M. J. Kim, S. A. Park, *et al.*, Soft-template synthesis of mesoporous non-precious metal catalyst with Fe-Nx/C active sites for oxygen reduction reaction in fuel cells., *Appl. Catal., B*, 2018, **222**, 191–199.
37 X. Xu, C. Xu, J. Liu, *et al.*, The synergistic effect of "soft-hard template" to in situ regulate mass transfer and defective sites of doped-carbon nanostructures for catalysis of oxygen reduction, *J. Alloys Compd.*, 2023, **939**, 168782.
38 C. Ouyang and X. Wang, Recent progress in pyrolyzed carbon materials as electrocatalysts for the oxygen reduction reaction, *Inorg. Chem. Front.*, 2019, **7**, 28–36.
39 Y. Persky, L. Kielesiński, S. N. Reddy, *et al.*, Biomimetic Fe–Cu porphyrrole aerogel electrocatalyst for oxygen reduction reaction, *ACS Catal.*, 2023, **13**, 11012–11022.
40 L. Peles-Strahl, H. C. Honig, Y. Persky, *et al.*, Modular Iron–Bipyridine-Based Conjugated Aerogels as Catalysts for

Oxygen Reduction Reaction, *ACS Catal.*, 2023, **13**, 14377–14384.
41 N. Zion, J. C. Douglin, D. A. Cullen, *et al*, Porphyrin aerogel catalysts for oxygen reduction reaction in anion-exchange membrane fuel cells, *Adv. Funct. Mater.*, 2021, **31**, 2100963.
42 S. Wu, X. Qu, J. Zhu, *et al.*, Recent advances in metal-organic frameworks derived electrocatalysts for oxygen reduction reaction, *J. Alloys Compd.*, 2024, **970**, 172518.
43 Y. Liu, Y. Wang, S. Zhao, *et al.*, Metal–organic framework-based nanomaterials for electrocatalytic oxygen evolution, *Small Methods*, 2022, **6**, 2200773.
44 M. Muhyuddin, S. Mostoni, H. C. Honig, *et al.*, Enhancing Electrocatalysis: Engineering the Fe–N x–C Electrocatalyst for Oxygen Reduction Reaction Using Fe-Functionalized Silica Hard Templates, *ACS Appl. Energy Mater.*, 2024, **7**, 11691–11702.
45 S. Akula, M. Mooste, J. Kozlova, *et al.*, Transition metal (Fe, Co, Mn, Cu) containing nitrogen-doped porous carbon as efficient oxygen reduction electrocatalysts for anion exchange membrane fuel cells, *Chem. Eng. J.*, 2023, **458**, 141468.
46 M. Muhyuddin, A. Friedman, F. Poli, *et al.*, Lignin-derived bimetallic platinum group metal-free oxygen reduction reaction electrocatalysts for acid and alkaline fuel cells, *J. Power Sources*, 2023, **556**, 232416.
47 S. A. Mirshokraee, M. Muhyuddin, J. Orsilli, *et al.*, Mono-, bi- and tri-metallic Fe-based platinum group metal-free electrocatalysts derived from phthalocyanine for oxygen reduction reaction in alkaline media, *Nanoscale*, 2024, **16**, 6531–6547.
48 G. Landrot and E. Fonda, Fastosh: a software for the treatment of XAFS datasets of environmental relevance or acquired in operando conditions, *J. Synchrotron Radiat.*, 2025, **32**, 1085–1094.
49 L. Minnetti, F. Paparoni, A. Zitolo, *et al.*, Elucidating hindered reactivity of high-manganese content mixed-olivine cathodes for Na-ion batteries: an operando X-ray absorption study, *Acta Mater.*, 2025, **301**, 121518.
50 H. J. Choi, G. Kwag and S. Kim, Electrochemical and XAFS investigation of nitrite reduction by heat-treated μ-oxo derivative of iron phthalocyanine supported on high area carbon, *J. Electroanal. Chem.*, 2001, **508**, 105–114.
51 W. Chen, M. Gong, K. Li, M. Xia, *et al.*, Insight into KOH activation mechanism during biomass pyrolysis: Chemical reactions between O-containing groups and KOH, *Appl. Energy*, 2020, **278**, 115730.
52 G. Kresse and J. Furthmüller, Efficiency of ab-initio total energy calculations for metals and semiconductors using a plane-wave basis set, *Comput. Mater. Sci.*, 1996, **6**, 15–50.
53 G. Kresse and J. Hafner, Ab initio molecular-dynamics simulation of the liquid-metal–amorphous-semiconductor transition in germanium, *Phys. Rev. B: Condens. Matter Mater. Phys.*, 1994, **49**, 14251.
54 G. Kresse and J. Hafner, Ab initio molecular dynamics for liquid metals, *Phys. Rev. B: Condens. Matter Mater. Phys.*, 1993, **47**, 558.
55 J. P. Perdew, K. Burke and M. Ernzerhof, Generalized gradient approximation made simple, *Phys. Rev. Lett.*, 1996, **77**, 3865.
56 P. E. Blöchl, Projector augmented-wave method, *Phys. Rev. B: Condens. Matter Mater. Phys.*, 1994, **50**, 17953.
57 G. Kresse and D. Joubert, From ultrasoft pseudopotentials to the projector augmented-wave method, *Phys. Rev. B: Condens. Matter Mater. Phys.*, 1999, **59**, 1758.
58 S. Grimme, J. Antony, S. Ehrlich, *et al.*, A consistent and accurate ab initio parametrization of density functional dispersion correction (DFT-D) for the 94 elements H-Pu, *J. Chem. Phys.*, 2010, **132**, 154104.
59 H. J. Monkhorst and J. D. Pack, Special points for Brillouin-zone integrations, *Phys. Rev. B: Solid State*, 1976, **13**, 5188.
60 C. Adamo and V. Barone, Toward reliable density functional methods without adjustable parameters: The PBE0 model, *J. Chem. Phys.*, 1999, **110**, 6158–6170.
61 G. Di Liberto, L. A. Cipriano and G. Pacchioni, Universal principles for the rational design of single atom electrocatalysts? Handle with care, *ACS Catal.*, 2022, **12**, 5846–5856.
62 D. Misra, G. Di Liberto and G. Pacchioni, CO_2 electroreduction on single atom catalysts: the role of the DFT functional, *Phys. Chem. Chem. Phys.*, 2024, **26**, 10746–10756.
63 J. K. Nørskov, J. Rossmeisl, A. Logadottir, *et al.*, Origin of the overpotential for oxygen reduction at a fuel-cell cathode, *J. Phys. Chem. B*, 2004, **108**, 17886–17892.
64 J. K. Nørskov, T. Bligaard, A. Logadottir, *et al.*, Trends in the exchange current for hydrogen evolution, *J. Electrochem. Soc.*, 2005, **152**, J23–J26.
65 E. Di Simone, G. Vile and G. Di Liberto, *et. al*, Decoding the role of adsorbates entropy in the reactivity of single-atom catalysts, *ACS Catal.*, 2025, **15**, 447–456.
66 C. Zhu, Q. Shi, B. Z. Xu, *et al.*, Hierarchically Porous M–N–C (M = Co and Fe) Single-Atom Electrocatalysts with Robust MNx Active Moieties Enable Enhanced ORR Performance, *Adv. Energy Mater.*, 2018, **8**, 1801226.
67 M. Muhyuddin, E. Berretti, S. A. Mirshokraee, *et al.*, Formation of the active site structures during pyrolysis transformation of Fe-phthalocyanine into Fe-N_x-C electrocatalysts for the oxygen reduction reaction, *Appl. Catal., B*, 2024, **343**, 123515.
68 I. A. Masashi Ishii, *XAFS Spectrum of Iron(II) Phthalocyanine*, SPring-8, 2021, DOI: 10.48505/nims.2039.
69 Y. Pan, Y. Chen, K. Wu, *et al.*, Regulating the coordination structure of single-atom Fe-N_xC_y catalytic sites for benzene oxidation, *Nat. Commun.*, 2019, **10**, 4290.
70 Y. Zhou, R. Lu, X. Tao, *et al*, Boosting Oxygen Electrocatalytic Activity of Fe–N–C Catalysts by Phosphorus Incorporation, *J. Am. Chem. Soc.*, 2023, **145**, 3647–3655.
71 V. C. A. Ficca, M. Sbroscia, E. Stellino, *et al.*, Non-Chemical Route to PGM-Free *via* N^+ Ion Implantation in Vertically Aligned Carbon Nanotubes, *Adv. Funct. Mater.*, 2025, **35**, 2413308.
72 G. Zuccante, M. Muhyuddin, V. C. A. Ficca, *et al.*, Transforming cigarette wastes into oxygen reduction

reaction electrocatalyst: does each component behave differently? An experimental evaluation, *ChemElectroChem*, 2024, **11**, e202300725.

73 B. Ricciardi, W. D. S. Freitas, B. Mecheri, *et al.*, Hierarchical porous Fe/Ni-based bifunctional oxygen electrocatalysts for rechargeable zinc-air batteries, *Carbon*, 2024, **219**, 118781.

74 M. Rahimihaghighi, M. Gigli, V. C. A. Ficca, *et al.*, Lignin-Derived Sustainable Nano-Platforms: A Multifunctional Solution for an Efficient Dye Removal, *ChemSusChem*, 2024, **17**, e202400841.

75 L. Sallaku, L. Mirizzi, M. Muhyuddin, *et al.*, Upgrading the waste Acrylonitrile-Butadiene-Styrene into crude oil and highly efficient electrocatalysts for oxygen reduction reaction, *Chem. Eng. J.*, 2025, **512**, 162236.

76 V. C. A. Ficca, C. Santoro, E. Placidi, *et al.*, Exchange current density as an effective descriptor of poisoning of active sites in platinum group metal-free electrocatalysts for oxygen reduction reaction, *ACS Catal.*, 2023, **13**, 2162–2175.

77 W. da Silva Freitas, B. Mecheri, C. L. Vecchio, *et al.*, Metal-organic-framework-derived electrocatalysts for alkaline polymer electrolyte fuel cells, *J. Power Sources*, 2022, **550**, 232135.

78 B. Mecheri, V. C. A. Ficca, M. A. C. de Oliveira, *et al.*, Facile synthesis of graphene-phthalocyanine composites as oxygen reduction electrocatalysts in microbial fuel cells, *Appl. Catal., B*, 2018, **237**, 699–707.

79 W. da Silva Freitas, A. D'Eepifanio, V. C. A. Ficca, *et al.*, Tailoring active sites of iron-nitrogen-carbon catalysts for oxygen reduction in alkaline environment: Effect of nitrogen-based organic precursor and pyrolysis atmosphere, *Electrochim. Acta*, 2021, **391**, 138899.

80 B. Ricciardi, B. Mecheri, W. da Silva Freitas, *et al.*, Porous iron-nitrogen-carbon electrocatalysts for anion exchange membrane fuel cells (AEMFC), *ChemElectroChem*, 2023, **10**, e202201115.

81 W. da Silva Freitas, A. D'Epifanio, C. Lo Vecchio, *et al.*, Tailoring MOF structure *via* iron decoration to enhance ORR in alkaline polymer electrolyte membrane fuel cells, *Chem. Eng. J.*, 2023, **465**, 142987.

82 L. Mirizzi, M. Muhyuddin, C. Lo Vecchio, *et al.*, Amorphous nanostructured Ni–Fe oxide as a notably active and low-cost oxygen evolution reaction electrocatalyst for anion exchange membrane water electrolysis, *Ind. Chem. Mater.*, 2025, **3**, 485–497.

83 M. Montalto, W. da Silva Freitas, E. Mastronardo, *et al.*, Spinel-type high-entropy oxides for enhanced oxygen evolution reaction activity in anion exchange membrane water electrolyzers, *Chem. Eng. J.*, 2025, **507**, 160641.

84 M. C. Biesinger, B. P. Payne, A. P. Grosvenor, *et al.*, Resolving surface chemical states in XPS analysis of first row transition metals, oxides and hydroxides: Cr, Mn, Fe, Co and Ni, *Appl. Surf. Sci.*, 2011, **257**, 2717–2730.

85 A. P. Grosvenor, B. A. Kobe, M. C. Biesinger, *et al.*, Investigation of multiplet splitting of Fe 2p XPS spectra and bonding in iron compounds, *Surf. Interface Anal.*, 2004, **36**, 1564–1574.

86 I. Barlocco, M. Spotti, G. Di Liberto, *et al.*, Electrochemical Nitrogen Reduction Reaction from Ab Initio Thermodynamics: Single versus Dual Atom Catalysts, *Adv. Theory Simul.*, 2024, **7**, 2400536.

87 M. Spotti, K. Maineri, F. Vines, *et al.*, Scaling relations and catalytic descriptor for the nitrogen reduction on single-atom catalysts, *Electrochim. Acta*, 2025, **542**, 147389.

88 F. Calle-Vallejo, M. Huang, J. B. Henry, *et al.*, Theoretical design and experimental implementation of Ag/Au electrodes for the electrochemical reduction of nitrate, *Phys. Chem. Chem. Phys.*, 2013, **15**, 3196–3202.

89 S. Emken, G. Di Liberto and G. Pacchioni, CO_2 electroreduction on single atom catalysts: Role of the local coordination, *Electrochim. Acta*, 2024, **499**, 144714.

90 W. Tang, E. Sanville and G. Henkelman, A grid-based Bader analysis algorithm without lattice bias, *J. Phys.: Condens. Matter*, 2009, **21**, 084204.

91 G. Henkelman, A. Arnaldsson and H. Jónsson, A fast and robust algorithm for Bader decomposition of charge density, *Comput. Mater. Sci.*, 2006, **36**, 354–360.

92 R. F. W. Bader, Atoms in molecules, *Acc. Chem. Res.*, 1985, **18**, 9–15.

93 E. Sanville, S. D. Kenny, R. Smith, *et al.*, Improved Grid-Based Algorithm for Bader Charge Allocation, *J. Comput. Chem.*, 2007, **28**, 899–908.

94 L. Liu, X. Zhao, H. Fu, *et al.*, Construction and identification of highly active single-atom Fe1-NC catalytic site for electrocatalytic nitrate reduction, *Appl. Catal., B*, 2023, **323**, 122171.

95 M. Zafari, M. Umer, A. S. Nissimagoudar, *et al.*, Unveiling the Role of Charge Transfer in Enhanced Electrochemical Nitrogen Fixation at Single-Atom Catalysts on BX Sheets (X = As, P, Sb), *J. Phys. Chem. Lett.*, 2022, **13**, 4530–4537.